Magnetic proximity effect and spin-orbital texture at the Bi₂Se₃/EuS interface

Alex Taekyung Lee[*]

Department of Physics, Korea Advanced Institute of Science and Technology (KAIST), Daejeon 305-701, Korea

Myung Joon Han[†]

*Department of Physics and KAIST Institute for the NanoCentury, Korea Advanced Institute of Science and Technology,
Daejeon 305-701, Korea*

Kyungwha Park[‡]

Department of Physics, Virginia Tech, Blacksburg, Virginia 24060, USA

We investigate a magnetic proximity effect on the Dirac surface states of a topological insulator (TI) induced by a Bi₂Se₃/EuS interface, using density-functional theory (DFT) and a low-energy effective model, motivated by a recent experimental realization of the interface. We consider a thin ferromagnetic insulator EuS film stacked on top of Bi₂Se₃(111) slabs of three or five quintuple layers (QLs) with the magnetization of EuS normal to the interface (z axis), which breaks time-reversal symmetry. It is found that a charge transfer and surface relaxation makes the Dirac cones electron doped. For both three and five QLs, the top-surface Dirac cone has an energy gap of 9 meV, while the bottom-surface Dirac cone remains gapless. This feature is due to the short-ranged induced magnetic moment of the EuS film. For the five QLs, an additional Dirac cone with an energy gap of 2 meV is formed right below the bottom-surface Dirac point, while for three QLs, there is no additional Dirac cone. We also examine the spin-orbital texture of the Dirac surface states with broken time-reversal symmetry, using DFT and the effective model. We find that the p_z orbital is coupled to the z component of the spin moment in the opposite sign to the p_x and p_y orbitals. The p_z and radial p orbitals are coupled to the in-plane spin texture in the opposite handedness to the tangential p orbital. The result obtained from the effective model agrees with our DFT calculations. The calculated spin-orbital texture may be tested from spin-polarized angle-resolved photoemission spectroscopy.

I. INTRODUCTION

Topological insulators (TIs) are distinguishable from ordinary insulators in that Dirac surface states are topologically protected by time-reversal symmetry and they have helical spin texture [1,2]. When TIs are interfaced with magnetic substrates or doped with magnetic elements, time-reversal symmetry can be broken. As a result, not only an energy gap is open at the Dirac point [3], but also various interesting effects are expected, such as the topological magnetoelectric effect [2], the quantum anomalous Hall effect [4,5], weak localization behavior in transport [6–8], and enhanced spin transfer torque [9,10].

Despite the previous studies on magnetic TIs, there remain several important issues that need to be resolved. First, when a TI is in contact with a ferromagnetic material, the coupling between them may not be weak. Consequently, the magnetic material may become nonmagnetic at the interface [11] or the magnetic substrate bands can be dominant near the Fermi level with the absence of TI surface states [12]. Second, when magnetic atoms such as Fe or Cr were doped in a TI [11,13–15], it was reported that the dopants may form clusters rather than being uniformly distributed without ferromagnetic ordering [15]. Last, the magnetic easy axis

of a magnetic TI may not be perpendicular to the surface [16].

Considering these issues, an interface between a ferromagnetic insulator (FMI) and a TI with a magnetic easy axis normal to the surface, is a good candidate system to study the magnetic proximity effect [12,17–19]. In this regard, a superlattice of Bi₂Se₃ (TI) interfaced with MnSe (FMI) in the presence of inversion symmetry (IS) was theoretically studied [12,17]. In this case, the Dirac surface states identified in Ref. [12] are not truly TI surface states because the TI surface-surface hybridization greatly increases with decreasing the FMI thickness. The large modification of the Dirac surface states by the FMI is consistent with the result in Ref. [17]. In addition, the Bi₂Se₃/MnSe interface has not been experimentally realized yet, and it has a lattice mismatch of 1.9%. Recently, the Bi₂Se₃/EuS interface has been fabricated and their transport properties have been measured [18,19], where the lattice mismatch is less than 1% and the structure has the magnetic easy axis normal to the interface (z axis). There are no theoretical studies of the magnetic proximity effect at this interface yet.

One interesting feature of the TI arising from strong spin-orbit coupling (SOC) is that the orbitals forming the topological surface states are highly coupled to a particular spin texture. This spin-orbital texture was studied for pristine TIs [20–22], and it was shown to be controlled by the polarization of incident photons [23,24]. Therefore, an interesting question is how the spin-orbital texture of

———————
[*]techlee@kaist.ac.kr
[†]mj.han@kaist.ac.kr
[‡]kyungwha@vt.edu

the surface states is modified by the magnetic proximity effect.

In this work, we present the spin-orbital texture and electronic structure of the surface states induced by the magnetic proximity effect at the Bi_2Se_3/EuS interface, using first-principles and effective model calculations. We consider a slab geometry where an EuS film with magnetic moment along the z axis is placed on top of Bi_2Se_3, which breaks both IS and time-reversal symmetry. The first-principles calculations show that three massive Dirac cones are present, and that EuS-dominated bands do not appear near the Fermi level. Among the three Dirac cones, the states localized into the top (bottom) TI surface have an energy gap of 9 meV (less than 1 meV), while a new Dirac cone slightly deeper into the top TI surface has an energy gap of 2 meV. By constructing a low-energy effective model for the surface states, we find that at small momentum the p_z orbital is coupled to the z component of the spin moment in the opposite sign to the p_x and p_y orbitals, while the p_z and radial p orbitals are coupled to the in-plane spin texture in the opposite handedness to the tangential p orbital. This result agrees with our first-principles calculations of the spin-orbital texture. The calculated spin-orbital texture can be observed from spin-polarized angle-resolved photoemission spectroscopy (ARPES).

II. FIRST-PRINCIPLES CALCULATION METHOD

We perform density-functional theory (DFT) calculations, using the projector augmented wave potentials [25] and generalized gradient approximation (GGA) [26] as an exchange-correlation functional, implemented in the VASP code [27]. We consider SOC self-consistently, where the spin quantization axis is the z axis. All Eu f electrons are taken as valence electrons. To include an additional correlation effect of Eu, we use $U_f = 8$ eV and $J_f = 1$ eV for Eu f orbitals within the GGA $+ U$ scheme [28]. Then we find that the optimized lattice constant of bulk EuS is 6.014 Å, and that the band gap is 1.12 eV comparable to the experimental value of 1.65 eV [29,30].

We consider a supercell where an EuS(111) film is on a Bi_2Se_3(111) slab of three or five quintuple layers (QLs) with a vacuum layer thicker than 40 Å. Note that in this slab geometry both IS and time-reversal symmetry are broken. With broken IS, the top-surface and bottom-surface Dirac cones are separated, resulting in gapless Dirac dispersion even for a Bi_2Se_3 slab as thin as two QLs [31]. This TI/FMI slab geometry can be taken as a "model" for experimental systems, considering that noncollinear magnetization and magnetic domains in EuS [18,19] are not included. However, in the first-principles calculations, the coupling between the topological surface states and bulklike states is inherently included as well as the coupling between surfaces, in contrast to the effective model for the surfaces [4]. At the Bi_2Se_3/EuS interface, we confirm that Se-Eu bonding is favorable over Se-S bonding, as expected from an ionic character of EuS and due to nominal valence states of Bi and Se. The topmost S atom in the Bi_2Se_3/EuS slab is passivated with H to avoid dangling bonds. We consider two configurations of the EuS film, such as Eu(1) at a fcc or hcp site of the TI slab. Relaxation of the slab geometry is carried out for both EuS
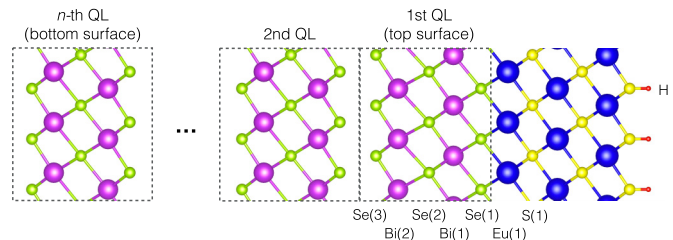

FIG. 1. (Color online) Schematic geometry of the Bi_2Se_3(111)/EuS(111) interface. The states localized into the first QL or the topmost QL are referred to as top-surface states.

configurations, until the forces on the EuS film and on the top four atomic layers in the TI slab [Bi(1), Se(1), Bi(2), and Se(2) in Fig. 1], are less than 0.01 eV/Å, while the rest of the atoms are fixed with the experimental values obtained from the experimental lattice constant of Bi_2Se_3, $a = 4.143$ Å [32]. We find that the fcc site gives an energy lower than the hcp site by 47 meV. Thus, henceforth, we consider only the fcc site for our calculations of band structures. The optimum Eu-Se bond length turns out to be 3.059 Å, which is similar to that in the bulk rocksalt EuSe [29]. Self-consistent calculations on the relaxed geometries are performed with an energy cutoff of 500 eV and $9 \times 9 \times 1$ k points until the total energy converges to 10^{-5} eV. Regarding dipole corrections, for three QLs, we confirm that they do not affect the band structure as long as the vacuum is thick enough.

III. ELECTRONIC STRUCTURE OF Bi_2Se_3/EuS

A. Results of 5-QL Bi_2Se_3

Figure 2(a) shows the calculated band structure of the 5-QL/EuS slab where the top and bottom TI surface states are marked in red and blue, and EuS bands in green. The top- and bottom-surface states are the ones where more than 40% of the electron density is localized into the topmost and bottommost QLs, respectively [33]. EuS-dominated states are defined as states with more than 30% of the density onto the EuS film. The exact percentages would not change the identification of the projected bands. A TI slab of five QLs has a weak surface-surface hybridization, considering that the decay length of the TI surface states is about two QLs (~ 2 nm).

The EuS bands are located outside the TI bulk band gap, and they are well separated from the top-surface and bottom-surface Dirac cones, as shown in Fig. 2(a). This is a distinctive feature of a TI/FMI interface and differs from the cases of metallic substrates or high concentrations of dopants or adatoms. One caveat is that two EuS bands appear close to the Fermi level E_F near the $\overline{M}$ point. These bands are expected to move further upward with on-site Coulomb repulsion for Eu d electrons (U_d) [30].

The calculated band structure shows three Dirac cones, while the pristine Bi_2Se_3 has two degenerate Dirac cones. The top-surface Dirac cone [labeled as III in Fig. 2(c)] is separated from the bottom-surface Dirac cone [labeled as I in Fig. 2(b)] due to broken IS. The top-surface (bottom-surface) cone has the binding energy of -0.812 eV (-0.234 eV). Here the binding energy is a difference between the Dirac point
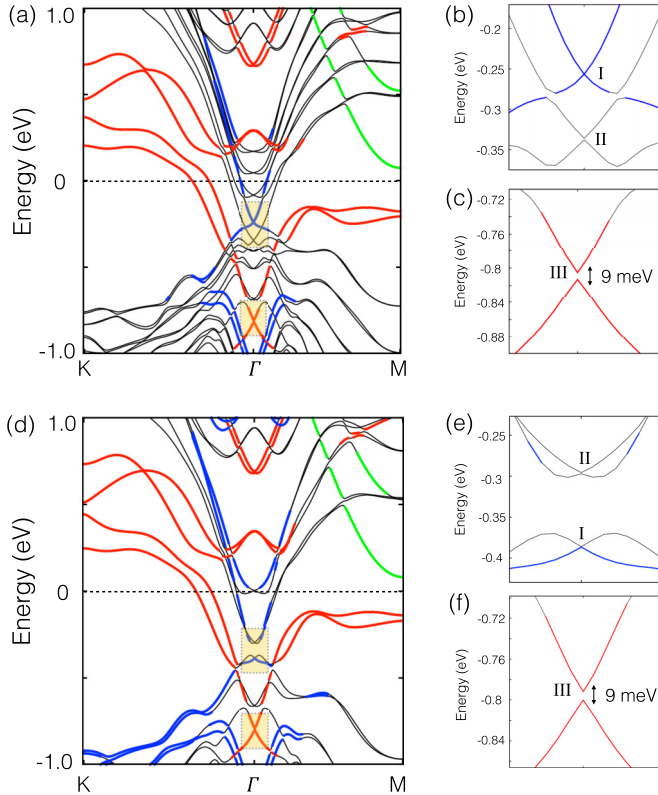
FIG. 2. (Color online) DFT-calculated band structure of the Bi$_2$Se$_3$/EuS slab when the TI slab is (a) five QLs or (d) three QLs, where the top-surface and bottom-surface states are marked in red and blue, respectively. Here the states in green are EuS bands, and the states in black are bulklike states. The definitions of the different types of the states can be found in the main text. The Fermi level E_F shown as the dashed lines are set to zero in energy. Several bands in the vicinity of the bottom-surface and top-surface Dirac points for the five QLs [(b),(c)] and the three QLs [(e),(f)], are highlighted.

FIG. 3. (Color online) (a) 5-QL/EuS slab geometry. (b) Charge transfer C_{net} as a function of z for the 5-QL/EuS slab. (c) Cumulative sum of the charge transfer vs z for the 5-QL/EuS slab. The vertical dashed lines separate adjacent QLs.

and E_F, which is defined in the previous report [34]. Right below the bottom-surface Dirac point, E_{DP}^b, a new Dirac cone [labeled as II in Fig. 2(b)] appears with the binding energy of -0.331 eV. The similar new Dirac cone was shown in the case of K adsorption [31].

The binding energies of the Dirac cones can be understood from a combination of surface relaxation and charge transfer. Let us first discuss the charge transfer effect. The amount of charge transfer is quantified from $C_{net}(z) = C[\text{Bi}_2\text{Se}_3/\text{EuS}] - C[\text{Bi}_2\text{Se}_3] - C[\text{EuS}]$, where $C[A]$ is charge of the slab geometry A, averaged over the xy plane. To estimate it, we perform self-consistent calculations using the same supercell size and DFT parameters and the relaxed geometry of the TI/FMI slab. As shown in Fig. 3(b), the values of $C_{net}(z)$ for the interfacial Eu and Se atoms, Eu(1) and Se(1), are negative and positive, respectively, suggesting that there must be a charge transfer from the EuS to the TI slab. By integrating $C_{net}(z)$ from $z = 0$ up to the midpoint of the Se(1) and Eu(1) positions, we obtain $0.092e$ per unit cell area, among which $0.0042e$ is transferred to the bottommost QL [Fig. 3(c)]. By filling the charge up in a Dirac cone with the Fermi velocity $v_F = 5 \times 10^5$ m/s [35,36] from the Dirac point, we estimate that the binding energies of the top-surface and bottom-surface
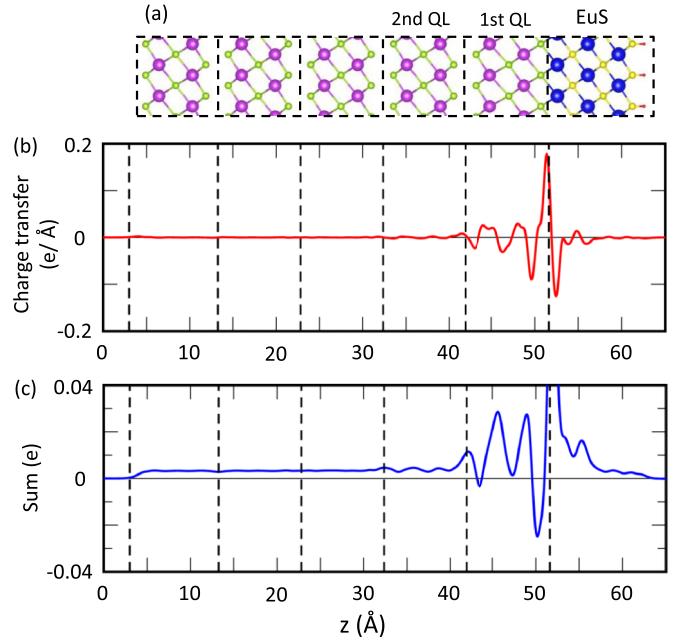
Dirac cones become about -0.9 eV and -0.2 eV, respectively. Then the effect of surface relaxation gives a small increase in the binding energy of the top-surface Dirac cone, while a small decrease in the binding energy of the bottom-surface Dirac cone.

We now discuss the energy gaps in the top-surface and bottom-surface Dirac cones followed by that in the new Dirac cone. The top-surface Dirac cone (labeled III in Fig. 2) has an energy gap of 9.0 meV, which can be understood from the following results: (i) a small amount of magnetic moment is induced only within the topmost QL; (ii) the top-surface states are mostly localized into the topmost QL with only 7% into the EuS film, as shown in Fig. 4(a). The magnetic moments of the interfacial Eu and the atoms in the topmost QL (labeled in Fig. 1) are as follows: $\mu[\text{Eu}(1)] = 6.793$, $\mu[\text{Se}(1)] = -0.024$, $\mu[\text{Bi}(1)] = 0.010$, $\mu[\text{Se}(2)] = -0.004$, $\mu[\text{Bi}(2)] = 0.004$, $\mu[\text{Se}(3)] = 0.004\mu_B$. The largest induced magnetic moment comes from Se(1), and the next largest moment from Bi(1). The fact that the largest induced moment is only $-0.024\mu_B$, is consistent with a highly localized character of Eu f electrons. The magnitude of the induced moment drops rapidly as the distance from the interface increases, and the direction of the moment alternates with the distance. The magnetic moment of the Eu(1) is slightly smaller than that of the bulk EuS, $6.962\mu_B$.

Our result of the top-surface cone differs from that at the Bi$_2$Se$_3$/MnSe interface [12,17] in three aspects. First, for the latter, the states giving the largest energy gap of about 50 meV, are localized mostly into the MnSe region and the interfacial Se atom, rather than into the topmost QL. In our case, not only the top-surface Dirac cone is localized into the topmost QL, but also the orbitals representing the Dirac cone are similar to
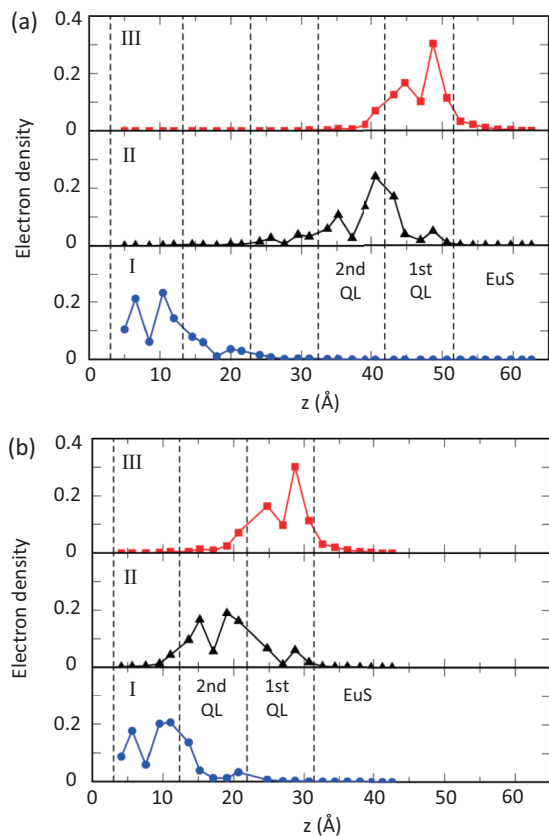
FIG. 4. (Color online) (a) Calculated electron density of the top-surface Dirac cone (top panel), new Dirac point (middle panel), and bottom-surface Dirac cone (bottom panel) at Γ for the 5-QL/EuS slab. (b) Calculated electron density of the top-surface Dirac cone, lowest-energy quantum-well states in the bulk conduction band region, and the bottom-surface Dirac cone at Γ for the 3-QL/EuS slab. The labels I, II, and III follow those in Fig. 2.

those for the top-surface and bottom-surface Dirac cones in a pristine Bi_2Se_3 slab. This feature is applied to not just near the Γ point but in the whole k space. Therefore, we claim that the top-surface Dirac cone still persists with a small energy gap upon EuS adsorption, although it appears with a large binding energy below the bulk valence band region. Secondly, for the Bi_2Se_3/MnSe interface, the induced magnetic moment was the largest for the topmost Bi atom from the interface ($0.04\mu_B$), while the magnetic moment of the topmost Se atom was less than $0.01\mu_B$. Thirdly, the Bi_2Se_3/MnSe system has some ambiguity in determination of an interface in comparison to our system, because the interfacial Se atom could be considered as part of both Bi_2Se_3 and MnSe.

The bottom-surface Dirac cone (labeled I) has an energy gap less than 1 meV, and it is mostly localized into the bottommost QL, as shown in Fig. 4(a). The small energy gap is due to the short-ranged induced magnetic moment from the EuS. Interestingly, just below the bottom-surface Dirac point, an additional Dirac cone [labeled II in Fig. 2(b)] with an energy gap of 2.0 meV appears. This new Dirac cone is localized slightly deeper into the TI slab and further away from the EuS film than the top-surface Dirac cone, as shown in the middle panel of Fig. 4(a). As a consequence, the magnetic moment

TABLE I. The Fermi level and the energies (in eV) of the top-surface and bottom-surface Dirac points $E_{DP}^{t,b}$, the new Dirac point E_{DP}^n, and two lowest-energy quantum-well states $E_{QWS1,QWS2}$ at $\overline{\Gamma}$ for the N QLs ($N = 3,5$) with the EuS film. Here E_{DP}^t is obtained from the midpoint of the gapped top-surface Dirac cone, and $V_1 = E_{DP}^b - E_{DP}^t$. Here the vacuum energy is set to zero.

N	E_F	E_{DP}^t	E_{DP}^b	V_1	E_{DP}^n	E_{QWS1}	E_{QWS2}
3	−5.222	−6.052	−5.639	0.413	N/A	−5.548	−5.250
5	−5.258	−6.070	−5.493	0.577	−5.589	−5.331	−5.204

induced into the new Dirac cone is fairly small, giving a smaller energy gap than the top-surface Dirac cone.

We discuss features of quantum-well states (QWSs) shown in the band structure Fig. 2(a). Near the Γ point, there are three QWSs with strong Rashba spin splitting in the bulk conduction band region and three QWSs in the bulk valence band region. The QWS right above the top-surface Dirac point has an energy gap of 2 meV at Γ, while the other five QWSs do not have an energy gap. Whether the QWSs are gapped or not, is determined by their electron density profiles. As momentum k increases from Γ, the QWSs in the bulk conduction band region become coupled to the bottom-surface Dirac cone, while the QWSs in the bulk valence band region are coupled to the top-surface Dirac cone. The absolute energies of two QWSs in the bulk conduction band region, QWS1 and QWS2, are listed in Table I. Interestingly, along $\overline{\Gamma K}$, E_F crosses six bands, while along $\overline{\Gamma M}$, E_F crosses four bands. The six bands are two top-surface states, a bottom-surface state, a new Dirac surface state, and the QWS1 pair, while the four bands are the bottom-surface state, the new Dirac surface state, and the QWS1 pair.

B. Effect of Bi_2Se_3 thickness

Now we examine an effect of TI slab thickness by computing the electronic structure of the 3-QL/EuS slab. As shown in Fig. 2(d), the top-surface Dirac cone has the binding energy of -0.830 eV, which is similar to that for the 5-QL/EuS case. This result is consistent with the observation that the charge transfer mostly occurs within the two to three QLs from the interface. On the other hand, the bottom-surface Dirac cone has the binding energy of -0.417 eV for the 3-QL/EuS slab, which is about 0.2 eV smaller than that for the 5-QL/EuS case. For the 3-QL case, the surface relaxation alone makes the bottom-surface Dirac cone more electron doped so that the binding energy becomes about -0.3 eV. Then the binding energy decreases slightly more due to a small charge transfer to the bottommost QL. The effect of surface relaxation is more prominent for a thinner slab.

Interestingly, in contrast to the 5-QL/EuS case, there are no new Dirac states for the 3-QL/EuS. This is due to the concerted effect of the charge transfer and surface relaxation. The states located at 0.09 eV above E_{DP}^b are QWS referred to as QWS1 with large Rashba spin splitting, labeled as II in Fig. 2(e) and listed in Table I. At small nonzero k values, the QWS1 are coupled to the bottom-surface states and open up a large gap of 78.4 meV. As k increases further, they are coupled to the top-surface states. Along $\overline{\Gamma K}$, E_F crosses two top-surface states, a bottom-surface state, one QWS1, and the QWS2 pair.

TABLE II. The hybridization gap 2Δ for the pristine N QLs ($N = 3,5$), and the energy gap of the top-surface Dirac cone for the N-QL/EuS slabs. Here $V_t = E_F - E_{DP}^t$ and $V_b = E_F - E_{DP}^b$.

N	2Δ	$2m$	V_t	V_b
3	0.036	0.009	0.830	0.417
5	0.006	0.009	0.812	0.234

The top-surface (bottom-surface) Dirac cone has an energy gap of 9 meV (less than 1 meV), similarly to the 5-QL case, although the surface-surface hybridization is stronger for the 3-QL slab (Δ in Table II). Our result is justified from the effective model discussed in Sec. IV A. The QWS1 has an energy gap of 1 meV, which is slightly smaller than that for the new Dirac cone for the 5-QL case. This difference can be due to the small difference in the electron density profile. Compare the middle panels in Figs. 4(a) and 4(b). The QWS1 for the 3-QL case is mostly localized into the second QL from the interface rather than the midpoint between the first and second QLs.

IV. MODEL HAMILTONIAN AND SPIN-ORBITAL TEXTURE

We construct a low-energy effective 4×4 Hamiltonian that can explain the DFT-calculated gaps of the surface-state Dirac cones, adapted from Ref. [4]. Then using this Hamiltonian, we investigate the spin-orbital texture of the surface states, and compare it with the DFT result.

A. Model Hamiltonian

The surface states at the Bi$_2$Se$_3$/EuS interface can be described by the following effective Hamiltonian:

$$H = \begin{pmatrix} H_R - V_t \boldsymbol{I} - \boldsymbol{M} \cdot \boldsymbol{\sigma} & \Delta \boldsymbol{I} \\ \Delta \boldsymbol{I} & -H_R - V_b \boldsymbol{I} \end{pmatrix}. \quad (1)$$

We use the basis set $\{|t\uparrow\rangle, |t\downarrow\rangle, |b\uparrow\rangle, |b\downarrow\rangle\}$, where t and b represent top-surface and bottom-surface states, and $\uparrow$ and $\downarrow$ refer to the electron spin directions along the $+z$ and $-z$ axes. Here the Rashba SOC Hamiltonian $H_R = \hbar v_F(\sigma_x k_y - \sigma_y k_x)$, where v_F is the Fermi velocity and $\boldsymbol{\sigma} = (\sigma_x, \sigma_y, \sigma_z)$ are the Pauli matrices. $\boldsymbol{I}$ is a 2×2 identity matrix. The binding energy of the top-surface (bottom-surface) Dirac cone is denoted as $-V_t$ ($-V_b$), where $V_b < V_t$, in order to incorporate the charge transfer. $\boldsymbol{M}$ is the effective exchange field from the EuS. Note that $\boldsymbol{M}$ is applied only to the top-surface states because this is a short-ranged proximity-induced field, not an ordinary magnetic field. The coupling between the top-surface and bottom-surface states gives an energy gap of 2Δ at Γ for a pristine thin TI slab.

The effective Hamiltonian differs from that in Refs. [20] in the sense that IS is broken via V_t, V_b, and $\boldsymbol{M}$. With an out-of-plane magnetization, $\boldsymbol{M} = m\hat{z}$ ($m > 0$), we find that eigenvalues of the Hamiltonian at $\mathbf{k} = 0$ are

$$\lambda_{1,2} = \frac{1}{2}[-V_2 \mp m - \sqrt{(V_1 \pm m)^2 + 4\Delta^2}],$$
$$\lambda_{3,4} = \frac{1}{2}[-V_2 \mp m + \sqrt{(V_1 \pm m)^2 + 4\Delta^2}], \quad (2)$$

where $V_1 = E_{DP}^b - E_{DP}^t$ and $V_2 \equiv V_t + V_b$. Here $\lambda_{1,2}$ correspond to pure top-surface states, while $\lambda_{3,4}$ correspond to pure bottom-surface states, when $\Delta = 0$.

Let us now assume that $\Delta, m \ll V_1$ for the 5-QL/EuS and 3-QL/EuS interfaces, which is consistent with the DFT result listed in Tables I and II . With this assumption, one can show that the surface-state energy gaps are, up to the order of $1/V_1^2$, written as

$$2m\left(1 - \frac{m^2}{4V_1^2} - \frac{\Delta^2}{V_1^2}\right), \quad 2m\left(\frac{m^2}{4V_1^2} + \frac{\Delta^2}{V_1^2}\right). \quad (3)$$

Therefore, as long as $m^2/V_1^2 \ll 1$ and $\Delta^2/V_1^2 \ll 1$ are satisfied, the Hamiltonian dictates that the top-surface energy gap is close to $2m$, while the bottom-surface energy gap is negligible. In addition, the surface-state energy gaps do not depend on TI slab thickness for slabs $\geqslant 3$ QLs, which agrees with the DFT calculations.

B. Spin-orbital texture

To examine the spin-orbital texture of the surface states, we consider the 5-QL/EuS since Δ for the 5-QL slab is negligible. Ignoring the surface-surface hybridization, we can describe low-energy properties of the top (bottom) surface states using the upper (lower) 2×2 block-diagonal matrix in Eq. (1). The spin-orbital texture of the bottom-surface states in our case is the same as that of a pristine TI slab [20] because $V_b \boldsymbol{I}$ in Eq. (1) does not affect the texture. Therefore, we first calculate the spin-orbital texture of the top-surface states using both the block-diagonal matrix and DFT. Then we present the texture of the new Dirac surface states by using DFT only. Note that the new Dirac surface states are localized deeper into the TI slab. The DFT calculations inherently include surface-bulk coupling, while the model Hamiltonian deals with surface states only. In this regard, the effective Hamiltonian has a limitation to study the new Dirac surface states.

1. Change of orbital and spin basis

The upper block-diagonal matrix, $H_R - V_t \boldsymbol{I} - \boldsymbol{M} \cdot \boldsymbol{\sigma}$, has two eigenvalues $\lambda_\pm = \pm\sqrt{m^2 + (\hbar v_F k)^2}$. The eigenvectors corresponding to the upper and lower Dirac cones of the top-surface states can be, respectively, written as

$$|\Phi_\pm\rangle = \frac{1}{N_\pm}(\pm i e^{-i\theta_k}\eta_\pm|\Psi_1\rangle + |\Psi_2\rangle), \quad (4)$$

where θ_k is the polar angle of an in-plane momentum vector $\vec{k}$, $\eta_\pm \equiv \hbar v_F k/(\pm\lambda_\pm \pm m)$, $k \equiv \sqrt{k_x^2 + k_y^2}$, and $N_\pm \equiv \sqrt{1 + \eta_\pm^2}$. With time-reversal symmetry, $\eta_\pm = 1$. Considering only p orbitals to the zeroth order in the $\mathbf{k} \cdot \mathbf{p}$ method, we use the basis functions such as

$$|\Psi_1\rangle = \sum_\alpha (u_\alpha|\alpha, p_z, \uparrow\rangle + v_\alpha|\alpha, p_+, \downarrow\rangle), \quad (5)$$

$$|\Psi_2\rangle = \sum_\alpha (u_\alpha|\alpha, p_z, \downarrow\rangle + v_\alpha|\alpha, p_-, \uparrow\rangle). \quad (6)$$

Here $|p_\pm\rangle = \mp(|p_x\rangle \pm i|p_y\rangle)/\sqrt{2}$. The basis functions $|\Psi_{1,2}\rangle$ form a time-reversal symmetry pair with the z component of

the total angular momentum $\pm 1/2$, respectively. Here u_α and v_α are material-dependent parameters for a pristine Bi_2Se_3 slab, and α represents atom indices. The values of u_α and v_α can be obtained from DFT calculations. However, as far as qualitative features of the spin-orbital texture are concerned, they are not needed. Our model differs from Ref. [20], in that $\eta_\pm \neq 1$ due to the broken time-reversal symmetry, and that the basis functions contain only the zeroth-order terms in the $\mathbf{k} \cdot \mathbf{p}$ method.

Now rewriting the eigenvectors $|\Phi_\pm\rangle$ in terms of p_z and radial and tangential p orbitals (p_r, p_θ), similarly to Ref. [20], we find

$$|\Phi_+\rangle = \frac{1}{N_+} \sum_\alpha \Big(u_\alpha \{ (\eta_+ + 1)|\alpha, p_z, \uparrow_\theta\rangle + (1 - \eta_+) $$

$$\times |\alpha, p_z, \downarrow_\theta\rangle\} - \frac{i}{\sqrt{2}} v_\alpha \{ (\eta_+ + 1)|\alpha, p_r, \uparrow_\theta\rangle $$

$$+ (\eta_+ - 1)|\alpha, p_r, \downarrow_\theta\rangle\} + \frac{1}{\sqrt{2}} v_\alpha \{ (\eta_+ - 1)|\alpha, p_\theta, \uparrow_\theta\rangle $$

$$+ (\eta_+ + 1)|\alpha, p_\theta, \downarrow_\theta\rangle\} \Big), \qquad (7)$$

$$|\Phi_-\rangle = \frac{1}{N_-} \sum_\alpha \Big(u_\alpha \{ (\eta_- + 1)|\alpha, p_z, \downarrow_\theta\rangle + (1 - \eta_-) $$

$$\times |\alpha, p_z, \uparrow_\theta\rangle\} + \frac{i}{\sqrt{2}} v_\alpha \{ (\eta_- + 1)|\alpha, p_r, \downarrow_\theta\rangle $$

$$+ (\eta_- - 1)|\alpha, p_r, \uparrow_\theta\rangle\} - \frac{1}{\sqrt{2}} v_\alpha \{ (\eta_- - 1)|\alpha, p_\theta, \downarrow_\theta\rangle $$

$$+ (\eta_- + 1)|\alpha, p_\theta, \uparrow_\theta\rangle\} \Big), \qquad (8)$$

where $|p_r\rangle = \cos\theta_k |p_x\rangle + \sin\theta_k |p_y\rangle$ and $|p_\theta\rangle = -\sin\theta_k |p_x\rangle + \cos\theta_k |p_y\rangle$. Figure 5 schematically shows how the radial and tangential p orbitals are related to the p_x and p_y orbitals. For example, the p_x orbital becomes tangential at $\theta_k = \pm\pi/2$, while it becomes radial at $\theta_k = 0$ and π. Here
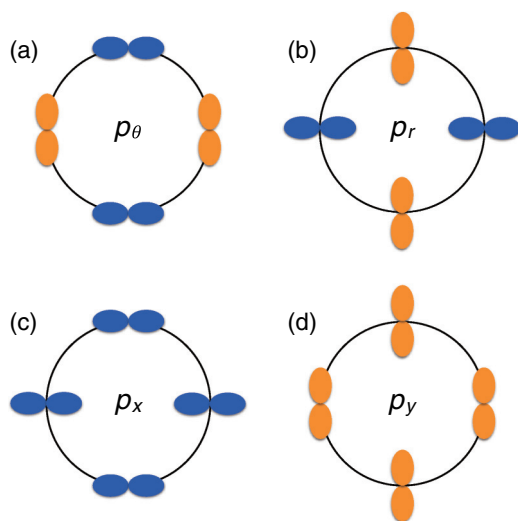

FIG. 5. (Color online) Schematic diagrams showing the relationships between two different in-plane orbital basis sets, (p_r, p_θ) and (p_x, p_y), where p_r and p_θ are radial and tangential p orbitals.

$|\uparrow_\theta\rangle = (1/\sqrt{2})(+ie^{-i\theta_k}|\uparrow\rangle + |\downarrow\rangle)$ represents the left-handed spin texture, where the spin magnetic moment rotates clockwise as θ_k increases. $|\downarrow_\theta\rangle = (1/\sqrt{2})(-ie^{-i\theta_k}|\uparrow\rangle + |\downarrow\rangle)$ represents the right-handed spin texture, where the spin moment rotates counterclockwise as θ_k increases. To compare with the DFT results, we project the wave functions, Eqs. (7) and (8), onto the orbital basis, p_x, p_y, and p_z, and calculate the expectation values of the x, y, and z components of the spin magnetic moment with respect to the projected wave functions, $\langle \sigma_{x,y,z} \rangle_{p_x, p_y, p_z}$.

2. Top-surface Dirac cone

We first examine the *upper* Dirac cone of the *top* surface states. The expectation values projected onto the $p_{x,y,z}$ orbitals are written as

$$\langle \sigma_z \rangle_{p_x,p_y} = \sum_\alpha v_\alpha^2 \frac{1 - \eta_+^2}{N_+^2}, \quad \langle \sigma_z \rangle_{p_z} = \sum_\alpha u_\alpha^2 \frac{\eta_+^2 - 1}{N_+^2}, \quad (9)$$

$$\langle \sigma_x \rangle_{p_x,p_y} = \mp \sum_\alpha v_\alpha^2 \frac{\eta_+}{N_+^2} \sin\theta_k, \quad \langle \sigma_x \rangle_{p_z} = \sum_\alpha u_\alpha^2 \frac{2\eta_+}{N_+^2} \sin\theta_k, \tag{10}$$

$$\langle \sigma_y \rangle_{p_x,p_y} = \mp \sum_\alpha v_\alpha^2 \frac{\eta_+}{N_+^2} \cos\theta_k,$$

$$\langle \sigma_y \rangle_{p_z} = -\sum_\alpha u_\alpha^2 \frac{2\eta_+}{N_+^2} \cos\theta_k, \tag{11}$$

where the minus (plus) sign on the left-hand side of Eqs. (10) and (11) is for p_x (p_y). DFT calculations are carried out at a small momentum k such as 0.0094 Å^{-1}, in order to avoid hexagonal warping effect. At this k point, $\eta_+ = 0.8654$, when we use $v_F = 5 \times 10^5$ m/s [35,36]. Figure 6 shows the DFT-calculated spin-orbital texture.

The projected z component of spin moment, Eq. (9), does not depend on θ_k, while the in-plane components, Eqs. (10) and (11), depend on θ_k. Figure 6 shows that $\langle \sigma_x \rangle_{p_x,p_y,p_z}$ is antisymmetric about the x axis, while $\langle \sigma_y \rangle_{p_x,p_y,p_z}$ is antisymmetric about the y axis. Thus, the projected x and y components of spin moment exactly follow the $\sin\theta_k$ and $\cos\theta_k$ dependence, respectively. Because $0 < \eta_+ < 1$, interestingly, $\langle \sigma_z \rangle_{p_z} < 0 < \langle \sigma_z \rangle_{p_x,p_y}$, as suggested from Eq. (9) and shown in the last column of Fig. 6.

Let us discuss the helicity of the in-plane spin texture coupled to the p_x, p_y, and p_z orbitals. For the p_z orbital, $\langle \sigma_x \rangle_{p_z}$ in Fig. 6(c) shows that the x component of spin moment points along the $+x$ axis at $\theta_k = \pi/2$, and along the $-x$ axis at $\theta_k = 3\pi/2$. $\langle \sigma_y \rangle_{p_z}$ in Fig. 6(c) shows that the y component of spin moment points along the $-y$ axis at $\theta_k = 0$, and the $+y$ axis at $\theta_k = \pi$. Thus, the spin moment coupled to the p_z orbital rotates clockwise, which implies left-handed spin texture. The spin texture coupled to the p_x and p_y orbitals can be, similarly, understood from Figs. 6(a) and 6(b) combined with Fig. 5. Using $\langle \sigma_x \rangle_{p_x}$ and $\langle \sigma_y \rangle_{p_y}$ in Fig. 6, we find that the tangential p orbital has right-handed spin texture. Similarly, we find that the radial p orbital has left-handed spin texture.

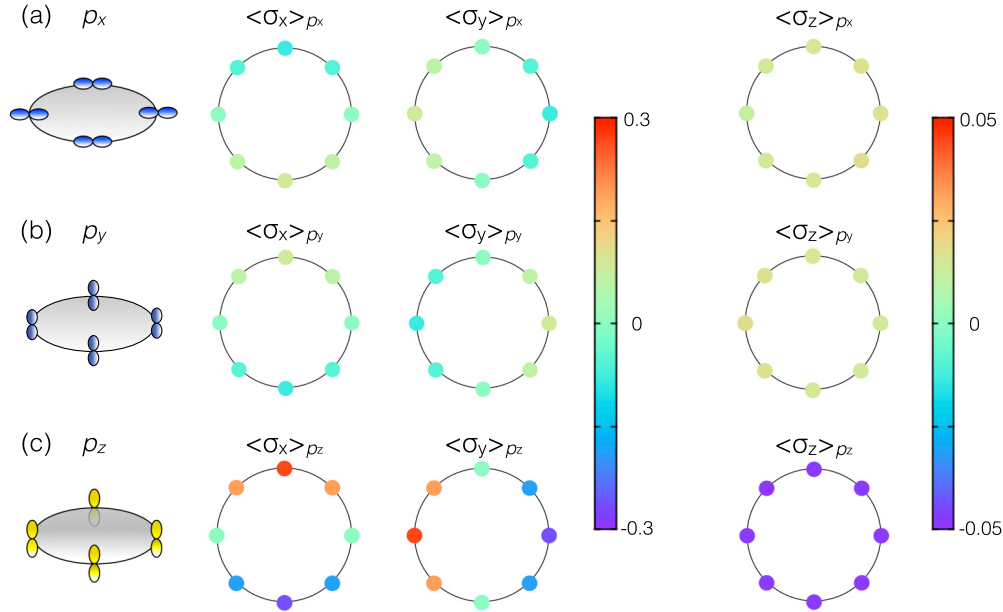Combining the results discussed so far, we discuss the overall spin-orbital texture. The DFT result gives

FIG. 6. (Color online) (a)–(c) Spin-orbital texture of the upper Dirac cone of the top-surface states in Bi_2Se_3/EuS at $k = 0.0094$ Å^{-1}, where the leftmost column shows the schematic figures of the p_x, p_y, and p_z orbitals. Note that $\langle\sigma_{x,y}\rangle$ have different scales from $\langle\sigma_z\rangle$.

$|\langle\sigma_z\rangle_{p_x,p_y}|/|\langle\sigma_z\rangle_{p_z}| = \sum_\alpha v_\alpha^2 / \sum_\alpha u_\alpha^2 = 0.3094$. As a result, the p_z orbital contributes dominantly to $\langle\sigma_z\rangle$ over the p_x and p_y orbitals. When this ratio is applied to Eqs. (10) and (11), we find that the contributions of the p_z orbital to $\langle\sigma_{x,y}\rangle$ are dominant over those of the p_x and p_y orbitals. In our case, η_+ is close to unity because $m \ll |\hbar v_F k|$ near Γ. Thus, Eqs. (9)–(11) imply that $|\langle\sigma_z\rangle_{p_z}|$ is smaller than the maximum value of $|\langle\sigma_{x,y}\rangle_{p_z}|$. This agrees with the DFT result, Fig. 6(c). Overall, the surface states in the upper Dirac cone have a strong left-handed in-plane spin texture with a small out-of-plane spin moment along the negative z axis, as shown in Fig. 6(c).

Our result differs from the spin-resolved ARPES data on Mn-doped Bi_2Se_3 [Figs. 3(e)–3(g) in Ref. [37]], where the spin texture was observed in the presence of a strong external magnetic field. First, the Bi_2Se_3 slab in the Bi_2Se_3/EuS interface responds diamagnetically to the weak exchange field from the EuS, while the Mn-doped Bi_2Se_3 does not have diamagnetic response to an external magnetic field. Note that the magnetization of the EuS film aligns along the positive z axis. The out-of-plane spin moment along the negative z axis is due to the diamagnetic response of Bi_2Se_3 to the ferromagnetic EuS film. The diamagnetic nature of Bi_2Se_3 has been shown in experiments [38,39]. Secondly, spin-orbital texture was not examined in the previous experiment [37].

Next, we examine the spin-orbital texture of the *lower* Dirac cone of the *top* surface states. In this case, the texture is the opposite to that of the upper Dirac cone discussed earlier. The expectation values are given as

$$\langle\sigma_z\rangle_{p_x,p_y} = \sum_\alpha v_\alpha^2 \frac{1-\eta_-^2}{N_-^2},$$

$$\langle\sigma_z\rangle_{p_z} = \sum_\alpha u_\alpha^2 \frac{\eta_-^2-1}{N_-^2}, \tag{12}$$

$$\langle\sigma_x\rangle_{p_x,p_y} = \pm\sum_\alpha v_\alpha^2 \frac{\eta_-}{N_-^2}\sin\theta_k,$$

$$\langle\sigma_x\rangle_{p_z} = -\sum_\alpha u_\alpha^2 \frac{2\eta_-}{N_-^2}\sin\theta_k, \tag{13}$$

$$\langle\sigma_y\rangle_{p_x,p_y} = \pm\sum_\alpha v_\alpha^2 \frac{\eta_-}{N_-^2}\cos\theta_k,$$

$$\langle\sigma_y\rangle_{p_z} = \sum_\alpha u_\alpha^2 \frac{2\eta_-}{N_-^2}\cos\theta_k, \tag{14}$$

where the plus (minus) sign on the left-hand side of Eqs. (13) and (14) is for p_x (p_y). DFT calculations are performed at $k = 0.0094$ Å^{-1}, and at this k point, $\eta_- = 1.1556$ using $v_F = 5 \times 10^5$ m/s [35,36]. Figure 7 shows the DFT-calculated spin-orbital texture.

Because of $\eta_- > 1$, $\langle\sigma_z\rangle_{p_x,p_y} < 0$ and $\langle\sigma_z\rangle_{p_z} > 0$ from Eq. (12) and shown in the last column of Fig. 7. This feature is the opposite to that in Fig. 6. The signs of $\langle\sigma_x\rangle_{p_x,p_y,p_z}$ ($\langle\sigma_y\rangle_{p_x,p_y,p_z}$) in Fig. 7 or Eqs. (13) and (14) are reversed to those in Fig. 6 or Eqs. (10) and (11) about the x axis (y axis). Therefore, the p_z and radial (tangential) orbitals are now coupled to the right- (left-)handed spin texture. Since the contributions of the p_z orbital are dominant over the p_x and p_y orbitals, overall, the surface states have right-handed in-plane spin texture with the out-of-plane spin moment along the positive z axis.

3. Bottom-surface Dirac cone

The proximity-induced effect does not influence the bottom-surface Dirac cone. Thus, $\eta_\pm = 1$, and Eqs. (9)–(14) give $\langle\sigma_z\rangle_{p_x,p_y,p_z} = 0$. Note that the bottom-surface Dirac cone is gapless within numerical accuracy. For the upper (lower) Dirac cone of the bottom-surface states, the p_x, p_y, and p_z or-
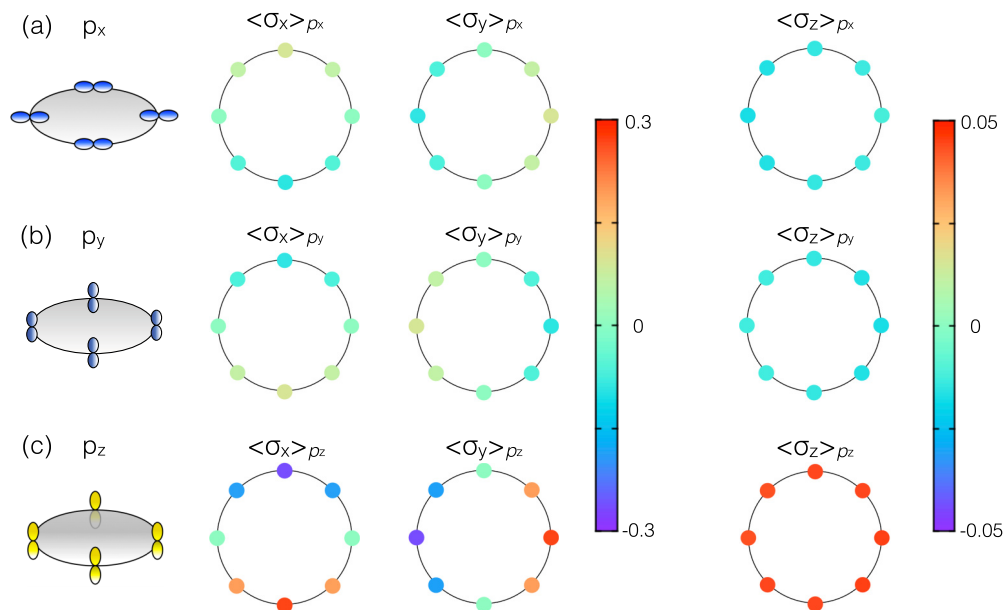
FIG. 7. (Color online) (a)–(c) Spin-orbital texture of the lower Dirac cone of the top-surface states in Bi_2Se_3/EuS at $k = 0.0094$ Å^{-1}.

bitals are coupled to the in-plane spin texture in the same fashion as those for the lower (upper) Dirac cone of the top-surface states. This agrees with our DFT calculations (not shown).

4. New Dirac cone

We also examine the the spin-orbital texture of the new Dirac cone appearing in the five QLs with EuS. The upper (lower) Dirac cone of the new surface states shows qualitatively similar spin-orbital texture to the upper (lower) Dirac cone of the top surface states. Three small quantitative differences are as follows. Compared to the top-surface states, (i) $|\langle \sigma_{x,y} \rangle_{p_z}|$ increases by $0.048 - 0.059 \mu_B$; (ii) $\langle \sigma_{x,y} \rangle_{p_x,p_y}$ decreases by $0.019 - 0.028 \mu_B$; (iii) $\langle \sigma_z \rangle_{p_z}$ and $\langle \sigma_z \rangle_{p_x,p_y}$ decrease by 0.022–0.028 and $0.007 - 0.012 \mu_B$, respectively, where the two different numbers for each difference come from the upper and lower Dirac cones. The differences in the x and y components of the spin moment arise because the orbitals of the new surface states slightly differ from those of the top-surface states. The new surface states have larger contributions from the p_z orbital and smaller contributions from the p_x and p_y orbitals than the top-surface states. The difference in the z component originates from the fact that the new Dirac surface states are localized slightly deeper into the TI slab, relative to the top- and bottom-surface states, as shown in Fig. 4. As a consequence, the proximity effect of the EuS film is weaker on the new Dirac surface states than on the top-surface states.

V. SUMMARY

In summary, we investigated the magnetic proximity effect on the electronic structure and spin-orbital texture of the Dirac surface states from the Bi_2Se_3/EuS slab through first-principles calculations and the effective model. The Dirac surface states localized into the QL right next to the interface, open up an energy gap of 9 meV, independently of the TI slab thickness for slabs as thick as three QLs or beyond. However, the Dirac surface states localized into the other side of the interface, remain gapless. These features of the gaps are due to the short-ranged induced magnetic moments into the TI slab. For the 5-QL/EuS slab, we found that a new Dirac cone was formed with an energy gap of 2 meV, while there was no such new Dirac cone for the 3-QL/EuS slab. We constructed the effective model Hamiltonian which includes surface-surface interaction, magnetic proximity effect, and band bending, in order to explain the gap of the top- and bottom-surface Dirac cones. By setting the spin-orbital basis for the model Hamiltonian, we computed the spin-orbital texture with broken time-reversal symmetry and this calculated result agrees with the DFT calculations.

[1] M. Z. Hasan and C. L. Kane, Rev. Mod. Phys. **82**, 3045 (2010).
[2] X.-L. Qi and S.-C. Zhang, Rev. Mod. Phys. **83**, 1057 (2011).
[3] Y. L. Chen, J.-H. Chu, J. G. Analytis, Z. K. Liu, K. Igarashi, H.-H. Kuo, X. L. Qi, S. K. Mo, R. G. Moore, D. H. Lu,

M. Hashimoto, T. Sasagawa, S. C. Zhang, I. R. Fisher, Z. Hussain, and Z. X. Shen, Science **329**, 659 (2010).
[4] R. Yu, W. Zhang, H.-J. Zhang, S.-C. Zhang, X. Dai, and Z. Fang, Science **329**, 61 (2010).

[5] C.-Z. Chang, J. Zhang, X. Feng, J. Shen, Z. Zhang, M. Guo, K. Li, Y. Ou, P. Wei, L.-L. Wang, Z.-Q. Ji, Y. Feng, S. Ji, X. Chen, J. Jia, X. Dai, Z. Fang. S.-C. Zhang, K. He, Y. Wang. L. Lu, X.-C. Ma, and Q.-K. Xue, Science **340**, 167 (2013).

[6] M. Liu, J. Zhang, C.-Z. Chang, Z. Zhang, X. Feng, K. Li, K. He, L.-l. Wang, X. Chen, X. Dai, Z. Fang, Q.-K. Xue, X. Ma, and Y. Wang, Phys. Rev. Lett. **108**, 036805 (2012).

[7] H.-T. He, G. Wang, T. Zhang, I.-K. Sou, G. K. L. Wong, J.-N. Wang, H.-Z. Lu, S.-Q. Shen, and F.-C. Zhang, Phys. Rev. Lett. **106**, 166805 (2011).

[8] H.-Z. Lu, J. Shi, and S.-Q. Shen, Phys. Rev. Lett. **107**, 076801 (2011).

[9] F. Mahfouzi, N. Nagaosa, and B. K. Nikolic, Phys. Rev. Lett. **109**, 166602 (2012).

[10] A. R. Mellnik, J. S. Lee, A. Richardella, J. L. Grab, P. J. Mintun, M. H. Fischer, A. Vaezi, A. Manchon, E.-A. Kim, N. Samarth, and D. C. Ralph, Nature **511**, 449 (2014).

[11] J. Li, Z. Y. Wang, A. Tan, P.-A. Glans, E. Arenholz, C. Hwang, J. Shi, and Z. Q. Qiu, Phys. Rev. B **86**, 054430 (2012).

[12] W. Luo and X.-L. Qi, Phys. Rev. B **87**, 085431 (2013).

[13] L. A. Wray, S.-Y. Xu, Y. Xia, D. Hsieh, A. V. Fedorov, H. Lin, A. Bansil, Y. S. Hor, R. J. Cava, and M. Z. Hasan, Nat. Phys. **7**, 32 (2011).

[14] T. Valla, Z.-H. Pan, D. Gardner, Y. S. Lee, and S. Chu, Phys. Rev. Lett. **108**, 117601 (2012).

[15] C.-Z. Chang, P. Tang, Y.-L. Wang, X. Feng, K. Li, Z. Zhang, Y. Wang, L.-L. Wang, X. Chen, C. Liu, W. Duan, K. He, X.-C. Ma, and Q.-K. Xue, Phys. Rev. Lett. **112**, 056801 (2014).

[16] F. Yang, Y. R. Song, H. Li, K. F. Zhang, X. Yao, C. Liu, D. Qian, C. L. Gao, and J.-F. Jia, Phys. Rev. Lett. **111**, 176802 (2013).

[17] S. V. Eremeev, V. N. Men'shov, V. V. Tugushev, P. M. Echenique, and E. V. Chulkov, Phys. Rev. B **88**, 144430 (2013).

[18] Q. I. Yang, M. Dolev, L. Zhang, J. Zhao, A. D. Fried, E. Schemm, M. Liu, A. Palevski, A. F. Marshall, S. H. Risbud, and A. Kapitulnik, Phys. Rev. B **88**, 081407(R) (2013).

[19] P. Wei, F. Katmis, B. A. Assaf, H. Steinberg, P. Jarillo-Herrero, D. Heiman, and J. S. Moodera, Phys. Rev. Lett. **110**, 186807 (2013).

[20] H. Zhang, C.-X. Liu, and S.-C. Zhang, Phys. Rev. Lett. **111**, 066801 (2013).

[21] Z.-H. Zhu, C. N. Veenstra, G. Levy, A. Ubaldini, P. Syers, N. P. Butch, J. Paglione, M. W. Haverkort, I. S. Elfimov, and A. Damascelli, Phys. Rev. Lett. **110**, 216401 (2013).

[22] Y. Cao, J. A. Waugh, X.-W. Zhang, J.-W. Luo, Q. Wang, T. J. Reber, S. K. Mo, Z. Xu, A. Yang, J. Schneeloch, G. D. Gu, M. Brahlek, N. Bansal, S. Oh, A. Zunger, and D. S. Dessau, Nat. Phys. **9**, 499 (2013).

[23] C.-H. Park and S. G. Louie, Phys. Rev. Lett. **109**, 097601 (2012).

[24] Chris Jozwiak, C.-H. Park, K. Gotlieb, C. Hwang, D.-H. Lee, S. G. Louie, J. D. Denlinger, C. R. Rotundu, R. J. Birgeneau, Z. Hussain, and A. Lanzara, Nat. Phys. **9**, 293 (2013).

[25] P. E. Blöchl, Phys. Rev. B **50**, 17953 (1994).

[26] J. P. Perdew, K. Burke, and M. Ernzerhof, Phys. Rev. Lett. **77**, 3865 (1996).

[27] G. Kresse and D. Joubert, Phys. Rev. B **59**, 1758 (1999).

[28] A. I. Liechtenstein, V. I. Anisimov, and J. Zaanen, Phys. Rev. B **52**, R5467 (1995).

[29] A. Jayaraman, A. K. Singh, A. Chatterjee, and S. Usha Devi, Phys. Rev. B **9**, 2513 (1974).

[30] D. B. Ghosh, M. De, and S. K. De, Phys. Rev. B **70**, 115211 (2004).

[31] K. Park, C. De Beule, and B. Partoens, New J. Phys. **15**, 113031 (2013).

[32] S. Nakajima, J. Phys. Chem. Solids. **24**, 479 (1963).

[33] K. Park, J. J. Heremans, V. W. Scarola, and D. Minic, Phys. Rev. Lett. **105**, 186801 (2010).

[34] Y. Xia, D. Qian, D. Hsieh, L. Wray, A. Pal, H. Lin, A. Bansil, D. Grauer, Y. S. Hor, R. J. Cava, and M. Z. Hasan, Nat. Phys. **5**, 398 (2009).

[35] H. J. Zhang, C.-X. Liu, X.-L. Qi, X. Dai, Z. Fang, and S.-C. Zhang, Nat. Phys. **5**, 438 (2009).

[36] C.-X. Liu, X.-L. Qi, H. J. Zhang, X. Dai, Z. Fang, and S.-C. Zhang, Phys. Rev. B **82**, 045122 (2010).

[37] S.-Y. Xu, M. Neupane, C. Liu, D. Zhang, A. Richardella, L. A. Wray, N. Alidoust, M. Leandersson, T. Balasubramanian, J. Sánchez-Barriga, O. Rader, G. Landolt, B. Slomski, J. H. Dil, J. Osterwalder, T.-R. Chang, H.-T. Jeng, H. Lin, A. Bansil, N. Samarth, and M. Z. Hasan, Nat. Phys. **8**, 616 (2012).

[38] M. Jain and A. Gupta, in *207 Diamagnetic Susceptibility of* Bi$_2$Se$_3$, edited by R. R. Gupta, Springer Materials—The Landolt-Bönstein Database (Springer-Verlag, Berlin/Heidelberg, 2007).

[39] H. Li, Y. R. Song, M.-Y. Yao, F. Zhu, C. Liu, C. L. Gao, J.-F. Jia, D. Qian, X. Yao, Y. J. Shi, and D. Wu, J. Appl. Phys. **113**, 043926 (2013).